A&A 675, A118 (2023)
https://doi.org/10.1051/0004-6361/202346517

Astronomy & Astrophysics

Radio continuum tails in ram pressure-stripped spiral galaxies: Experimenting with a semi-empirical model in Abell 2255

A. Ignesti[1], B. Vulcani[1], A. Botteon[2], B. Poggianti[1], E. Giunchi[1,3], R. Smith[4], G. Brunetti[2], I. D. Roberts[5], R. J. van Weeren[5], and K. Rajpurohit[6]

[1] INAF-Padova Astronomical Observatory, Vicolo dell'Osservatorio 5, 35122 Padova, Italy
e-mail: alessandro.ignesti@inaf.it
[2] INAF, Istituto di Radioastronomia di Bologna, Via Gobetti 101, 40129 Bologna, Italy
[3] Dipartimento di Fisica e Astronomia "Galileo Galilei", Universitá di Padova, Vicolo dell'Osservatorio 3, 35122 Padova, Italy
[4] Universidad Tècnica Federico Santa Marìa, Avda. Vicuña Mackenna 3939, Oficina A035, San Joaquìn, Santiago, Chile
[5] Leiden Observatory, Leiden University, PO Box 9513, 2300 RA Leiden, The Netherlands
[6] Harvard-Smithsonian Center for Astrophysics, 60 Garden Street, Cambridge, MA 02138, USA

Received 28 March 2023 / Accepted 31 May 2023

ABSTRACT

Context. Wide-field radio continuum observations of galaxy clusters are revealing an increasing number of spiral galaxies hosting tens of kiloparsec-length radio tails produced by the displacement of nonthermal interstellar medium (ISM) by ram pressure.
Aims. We present a semi-empirical model for the multifrequency radio continuum emission from ram-pressure-stripped tails based on the pure synchrotron cooling of a radio plasma moving along the stripping direction with a uniform velocity.
Methods. We combine LOFAR and uGMRT observations at 144 and 400 MHz to study the flux density and spectral index profiles of the radio tails of seven galaxies in Abell 2255, and use the model to reproduce the flux density and spectral index profiles, and infer the stripped radio plasma velocity.
Results. For five out of these seven galaxies, we observe a monotonic decrease in both flux density and spectral index up to 30 kpc from their stellar disk. Our model reproduces the observed trends with a projected radio plasma bulk velocity of between 160 and 430 km s^{-1}. This result represents the first indirect measurement of the stripped, nonthermal ISM velocity. The observed spectral index trends indicate that the synchrotron cooling is faster than the adiabatic expansion losses, suggesting that the stripped radio plasma can survive for a few tens of million years outside of the stellar disk. This provides a lower limit on the lifetime of the stripped ISM outside of the disk. As a proof of concept, we use the best-fit velocities to constrain the 3D velocity of the galaxies in the cluster to be in the range of 300−1300 km s^{-1}. We estimate the ram pressure affecting these galaxies to be between 0.1 and 2.9×10^{-11} erg cm^{-3}, and measure the inclination between their stellar disk and the ram pressure wind.

Key words. radio continuum: galaxies – galaxies: clusters: individual: Abell 2255 – methods: observational

1. Introduction

Galaxies in clusters can evolve from star-forming into passive systems (e.g., Dressler 1980; Blanton et al. 2009; Fasano et al. 2000; Cortese et al. 2021). One of the main drivers of this "environmental processing" is the interaction between the galaxy interstellar medium (ISM) and the intracluster medium (ICM) that fill the cluster volume. This physical interaction manifests as an external pressure exerted by the ICM, the so-called "ram pressure" $P_{\rm Ram}$, which can overcome the stellar disk binding force and strip the ISM components from the galaxy (Gunn & Gott 1972). This ram pressure stripping (RPS) can be crucial for the galaxy, as the gas loss can effectively quench the star formation in the stellar disk (Boselli et al. 2022, for a review), making it an important quenching pathway for satellite galaxies (e.g., Vollmer et al. 2001; Tonnesen et al. 2007; Vulcani et al. 2020; Watts et al. 2023). RPS is a frequent phenomenon, as almost all galaxies in clusters undergo a RPS event visible at optical wavelengths within their lifetime (Vulcani et al. 2022). The ram pressure action is not limited to displacing the ISM outside of the disk. The impact of ram pressure can result in many effects, including compression of gas along the leading edge of the disk (e.g., Rasmussen et al. 2006; Poggianti et al. 2019a; Roberts et al. 2022a), disturbed galaxy morphologies, and trailing tails of stripped gas (e.g., Kenney et al. 2004; van Gorkom 2004; Fumagalli et al. 2014; Poggianti et al. 2017a), and condensation of star-forming knots in the tails (Kenney et al. 2014; Poggianti et al. 2019b). It can also temporarily enhance the global star formation (e.g., Poggianti et al. 2016; Vulcani et al. 2018; Roberts & Parker 2020) and trigger the activity of the central nuclei (e.g., Poggianti et al. 2017b; Peluso et al. 2022). Indeed it has been observed that it can affect the microphysics of the ISM on small scales, for example by stimulating the conversion from atomic to molecular hydrogen (Moretti et al. 2020), enhancing the diffusivity of cosmic rays (Farber et al. 2022; Ignesti et al. 2022a), or by inducing mixing between the ISM and ICM (Sun et al. 2021; Franchetto et al. 2021). The most extreme examples of galaxies undergoing strong RPS are the so-called jellyfish galaxies (Fumagalli et al. 2014; Smith et al. 2010; Ebeling et al. 2014; Poggianti et al. 2017a). In the optical/UV band, these objects show extraplanar, unilateral debris extending beyond their stellar disks, and striking tails of ionised gas. Jellyfish galaxies mostly reside in galaxy clusters and are a transitional phase between infalling star-forming spirals and quenched cluster galaxies; for this reason, they provide a unique opportunity to understand the impact of gas-removal processes on galaxy evolution.

Table 1. Summary of the properties of A2255.

Property	Value
RA [°]	258.216
Dec [°]	+64.063
z	0.08012 ± 0.00024
σ_{cl} [km s^{-1}]	1137 ± 50
M_{500} [$\times 10^{14}$ $M_\odot$]	5.38 ± 0.06
R_{500} [Mpc]	1.196
R_{200} [Mpc]	2.033

Notes. From top to bottom: equatorial coordinates (Eckert et al. 2017); redshift z, and velocity dispersion σ_{cl} (Golovich et al. 2019); M_{500}, R_{500}, and R_{200} (Planck Collaboration XXVII 2016).

A number of jellyfish galaxies have been observed that show tails of radio continuum emission extending for tens of kiloparsecs (kpc) from their stellar disk (e.g., Gavazzi & Jaffe 1987; Murphy et al. 2009; Vollmer et al. 2013; Chen et al. 2020; Müller et al. 2021; Roberts et al. 2021, 2022b; Ignesti et al. 2022a). These radio tails typically develop steep-spectrum emission ($\alpha < -0.9$ at GHz frequencies) within few tens of kpc from the stellar disk (e.g., Vollmer et al. 2004; Chen et al. 2020; Ignesti et al. 2022b; Müller et al. 2021; Lal et al. 2022; Venturi et al. 2022). Therefore, they are best observed below GHz frequencies, and for this reason the ongoing LOFAR Two-metre Sky Survey (LoTSS, Shimwell et al. 2017, 2019, 2022), which provides high-resolution (6″) and highly sensitive (∼100 μJy beam^{-1}) images of the Northern sky at 120−168 MHz, is providing us with an increasing number of detections. Until now, about 100 spiral galaxies with RPS radio tails have been reported, and thanks to this relatively large sample size, it is now possible to conduct statistical studies of the RPS tail development in clusters (see Smith et al. 2022a, for a recent example). These "radio tails" are produced by cosmic ray electrons (CRe) accelerated to energies of a few GeV by supernova explosions in the stellar disk (Condon 1992). The relativistic plasma is then stripped, together with the ISM, from the disk by the ram pressure. The CRe cool down by emitting radio waves via synchrotron radiation until the stripped clouds evaporate in the ICM. The magnetic field of the stripped tail, which is responsible for the CRe synchrotron losses, can be further amplified by the ICM magnetic draping (Dursi & Pfrommer 2008; Pfrommer & Dursi 2010; Ruszkowski et al. 2014; Müller et al. 2021). This qualitative scenario is supported by multifrequency studies that observed a spectral index steepening with radial distance along these tails (e.g., Vollmer et al. 2004; Chen et al. 2020; Müller et al. 2021; Ignesti et al. 2022b; Roberts et al. 2022b; Venturi et al. 2022). In this framework, the length of the radio tail would be mainly driven by two factors, which are the synchrotron cooling time (Pacholczyk 1970), and the radio plasma bulk velocity, V, along the stripping direction. An interesting implication of this scenario is that, for the radio plasma to cool down mainly via synchrotron emission, the stripped ISM clouds should be able to survive in the ICM for a timescale that is at least as long as the radiative time. Constraining the lifetime of the stripped ISM clouds outside of the stellar disk is of value when investigating the origin of the extraplanar star formation of jellyfish galaxies, or when investigating general astrophysical problems such as the evolution of cold gas clouds in a hot wind.

In the present work, we develop a semi-empirical model to reproduce the radio tail of RPS galaxies and we test it on a sample of galaxies in the galaxy cluster Abell 2255 imaged with deep observations at 144 and 400 MHz. The manuscript is organized as follows. In Sect. 2 we present the sample and the data used for this analysis, and the model developed to reproduce them. The results are presented in Sect. 3 and discussed in Sect. 4, where we also present the caveats of our work. Throughout the paper, we adopt a ΛCDM cosmology with $\Omega_{DM} = 0.7$, $\Omega_{matter} = 0.3$, and $H_0 = 70\,\mathrm{km\,s^{-1}\,Mpc^{-1}}$, which yields $1'' = 1.512$ kpc at the cluster redshift ($z = 0.08012$; Golovich et al. 2019). We describe the radio synchrotron spectrum as $S \propto \nu^{\alpha}$, where S is the flux density, ν the frequency, and α is the spectral index.

2. Data analysis

2.1. Cluster properties and data preparation

We analyze the radio emission of a sample of galaxies in the galaxy cluster Abell 2255 (Abell 1958, hereafter A2255), a nearby system ($z = 0.08012$, Golovich et al. 2019) with a complex merger dynamics. Previous optical analyses suggested a merger along the line of sight, whereas the X-ray morphology, elongated along the E–W axis, points to a second merger in that direction (Yuan et al. 2003; Golovich et al. 2019). In the radio band, A2255 shows a diffuse radio halo at its center (reported for the first time by Jaffe & Rudnick 1979), and a large number of head–tail radio galaxies (e.g., Harris et al. 1980; Feretti et al. 1997; Miller & Owen 2003; Pizzo & de Bruyn 2009; Botteon et al. 2020a). Thanks to deep observations provided by the LOw Frequency ARray (LOFAR; van Haarlem et al. 2013), it has been revealed that A2255 hosts diffuse radio emission extending beyond R_{200} (Botteon et al. 2022). We summarize the properties of A2255 in Table 1.

This cluster is an ideal candidate for testing our model because of the availability of deep LOFAR and upgraded Giant Metrewave Radio Telescope (uGMRT) observations at 120−168 MHz and 400 MHz, respectively.

We make use of the 75 h LOFAR observation presented in Botteon et al. (2022, for a detailed description of the data calibration) to produce a new image at a central frequency of 144 MHz with a lower uvcut of 2000λ, `ROBUST` = −0.5 (Briggs & Cornwell 1994), and a taper of 5 arcsec. The image is centered on the cluster and covers an area of 1 deg^2. The imaging was carried out with the software `WSCLEAN` (Offringa et al. 2014). The resulting image, shown in Fig. 1, has an angular resolution of 10.3″×6.6″, and rms = 55 μJy beam^{-1}. The lower uvcut permits us to remove the radio emission diffused on scales larger than ∼100″ (∼150 kpc), and thus to reveal the smaller sources beneath, such as the radio tails.

A2255 was observed with the uGMRT in band 3 (300−500 MHz) for 40 h (project code: 39_032, PI: A. Botteon), and is presented here for the first time. The observations were divided into four runs of 10 h each, carried out on 2021 February 20, 26, March 13, and April 1, bookended by two 8 m scans on the flux density calibrators 3C 286 and 3C 48. The data were recorded in 2048 frequency channels with an integration time of 5.3 s using both the narrow-band (bandwidth of 33.3 MHz) and wide-band (bandwidth of 200 MHz) backends. The data were processed with the Source Peeling and Atmospheric Modeling (SPAM) package (Intema et al. 2009), which is widely used to reduce GMRT observations; SPAM performs calibration of the flux density scale, correction for the bandpass, data averaging and flagging, and direction-dependent calibration. In order to produce deep and wide-band images of A2255 at the central frequency of 400 MHz, we proceeded as follows. First, we processed the four narrow-band datasets independently to assess the

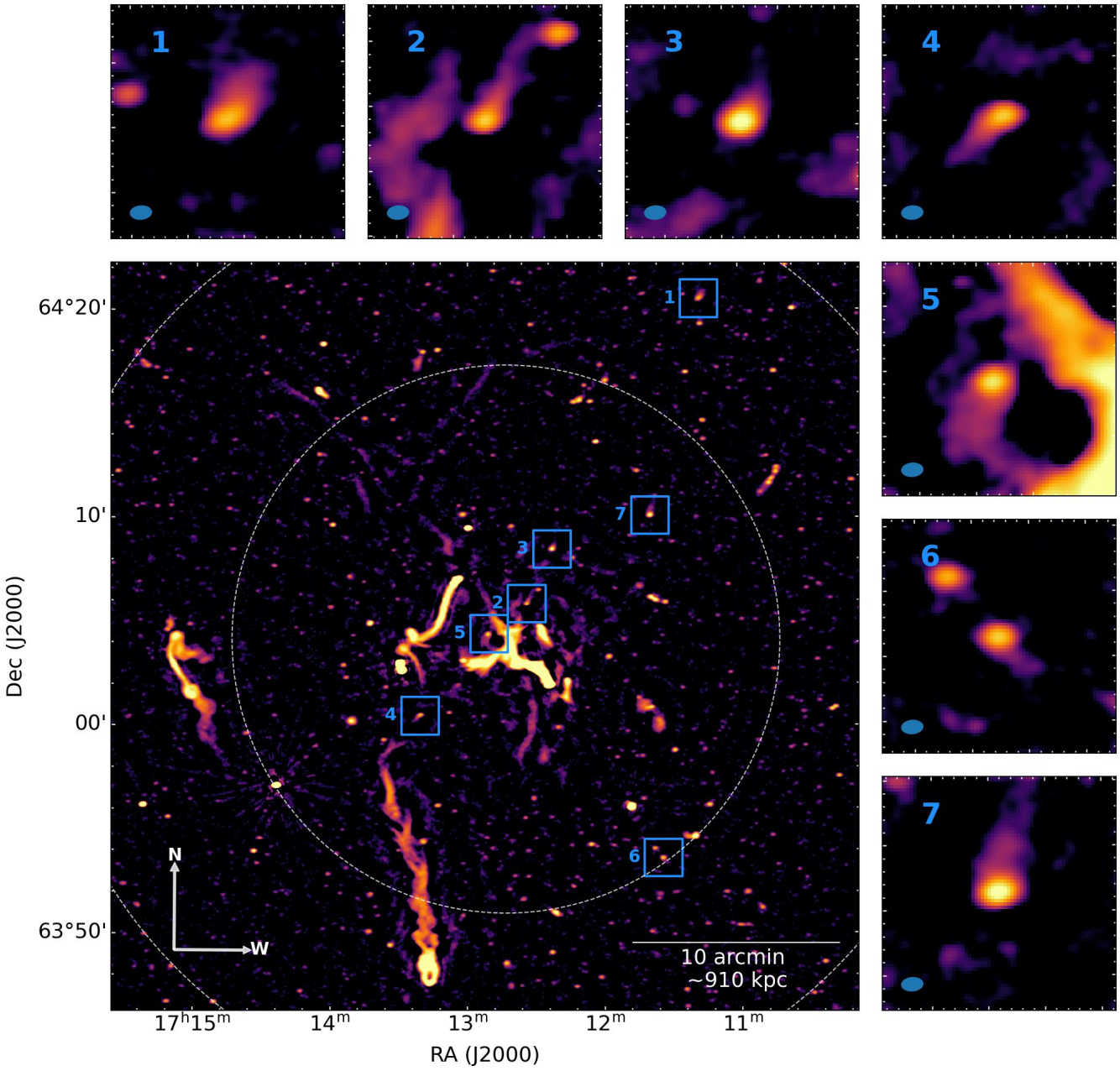

Fig. 1. LOFAR image at 144 MHz of A2255 obtained with a lower uvcut of 2000λ (rms = 55 μJy beam^{-1}, resolution 10.3″ × 6.6″). Inner and outer dashed circles show R_{500} = 1.196 Mpc and R_{200} = 2.033 Mpc, respectively. The blue boxes point out the seven galaxies analyzed in this work and shown in the seven small panels. The box size in the large panel corresponds to the FOV of the corresponding galaxy panel.

quality of the four observing runs. Second, we split each wide-band dataset into six slices with equal bandwidth of 33.3 MHz, from 300 to 500 MHz. This step is necessary for SPAM to handle the wide-band of the new uGMRT backend and has already been adopted in previous studies (e.g., Botteon et al. 2020b; Di Gennaro et al. 2021; Schellenberger et al. 2022). Third, we obtained a global sky model from the best narrow-band image (run of 2021 April 1) to jointly calibrate and merge the slices centered at the same frequency as the four observing runs. Fourth, we jointly deconvolved the six resulting calibrated slices with `WSClean`, enabling the multiscale multifrequency deconvolution (Offringa & Smirnov 2017). The resulting image, which was corrected for the primary beam response, has a resolution of 9.8″ × 9.0″ and an rms = 20 μJy beam^{-1}. In this paper, we focus on the jellyfish galaxies, while a forthcoming publication will focus on the diffuse radio emission (Rajpurohit et al., in prep.).

We also make use of images and spectroscopy from the 12th release of the Sloan Digital Sky Survey (SDSS; York et al. 2000). We combine SDSS images[1] in the *g*-, *r*-, and *i*-filter to produce color images of the cluster galaxies.

2.2. Galaxy sample selection

We select a sample of suitable galaxies for this analysis solely on the basis of their radio emission morphology. Specifically, we focus on those galaxies with an evident spiral or disk morphology in the SDSS image, and radio tails that are detected above

[1] From `https://dr12.sdss.org/mosaics/`

the 3×rms level and resolved by more than three resolution elements at 144 MHz. This latter condition is necessary to reliably sample their flux density profiles.

We end up with a sample of seven galaxies, which we show in Fig. 1. Their properties are summarized in Table 2. According to SDSS 16 classification (Ahumada et al. 2020), these galaxies are star-forming spirals without evidence of AGN activity. Hence, their radio tails should be produced solely by the interactions between the ram pressure winds and the CRe accelerated by the supernovae. All the galaxies have the radio tail pointing away from the cluster center, and, with the exception of #6, are remarkably aligned along the cluster NW–SE axis, which may suggest that they are collectively falling toward A2255 along a privileged direction. This piece of evidence might indicate that the NW–SE axis is critical for the ongoing merger, thus adding another piece of the puzzle that is the complex dynamics of this cluster. Finally, we note that all seven galaxies are blueshifted with respect to the cluster ($z < z_{\rm cl}$).

2.3. Analysis of the radio tails

2.3.1. Flux density and spectral index profiles

To evaluate the properties of the radio tails, we sample their radio emission in order to infer the flux density decline with distance. We define a grid composed of a set of aligned elliptical regions with a size of 11×7 arcsec^2 –thus larger than the beam sizes of the radio images– that start from the galaxy center and extend to the end of the tail as observed at 144 MHz. The first bin, located over the stellar disk, serves solely to define the galaxy position in the cluster, which is used to compute the projected length of the tail. For each radio map, we proceed by measuring the flux density in each elliptical region –beyond the first one– located over the corresponding 3σ contour, and we compute the corresponding uncertainty $\sigma = \sqrt{A/A_{\rm beam}} \times {\rm rms}$ (where A and $A_{\rm beam}$ are, respectively, the area of the sampling bin and the beam). We then measure the spectral index in each bin in which we observe emission both at 144 and 400 MHz as:

$$\alpha = \frac{\log\left(\frac{S_{144}}{S_{400}}\right)}{\log\left(\frac{144}{400}\right)} \pm \frac{1}{\log\left(\frac{144}{400}\right)} \sqrt{\left(\frac{\sigma_{144}}{S_{144}}\right)^2 + \left(\frac{\sigma_{400}}{S_{400}}\right)^2}, \quad (1)$$

where σ_{144} and σ_{400} are the flux density uncertainties at 144 and 400 MHz. Finally, in order to define the distance of each bin from the stellar disk, we consider the projected physical distance between the center of each bin and that of the previous one. This approach permits us to compute the position of each bin with respect to the stellar disk as the sum of the distances of the previous bins.

The projected length of the radio tail lies between 35 and 60 kpc, with galaxies showing different declining slopes. For galaxy #2, we adopt special considerations because the radio tail connects with another galaxy located toward the northwest (Fig. 1). The current image resolution does not allow us to distinguish whether the connection is real or just a blend of multiple sources. Regardless, we decide to sample its tail up to ∼40 kpc from the disk.

2.3.2. Modeling the multifrequency radio tail

We model the expected flux density and spectral index profiles by assuming that (i) they are produced by radio plasma clouds accelerated in the stellar disk, (ii) that these clouds move along the stripping direction with a uniform bulk velocity, and (iii) that the CRe cooling is dominated by synchrotron and inverse compton (IC) energy losses due to the Cosmic Microwave Background (CMB; e.g., Longair 2011). These assumptions are motivated by the fact that the stripped tails are mostly composed of ionized gas (e.g., Boselli et al. 2022), and therefore the CRe perceive a local gas density that is lower than that within the stellar disk ($n_{\rm gas} \sim 10^{-2}$–10^{-1} cm^{-3}). Under such conditions, the timescales of the other energy-loss mechanisms, such as ionization losses, bremmstrahlung radiation, or IC with the galactic radiation field, are of the order of a few gigayears (e.g., Basu et al. 2015, Eqs. (5)–(8)), and are therefore negligible with respect to synchrotron losses ($t \simeq 10^7$–10^8 yr). Our estimate is conservative because we assume a uniform magnetic field and we neglect adiabatic losses. The latter assumption is partially supported by the fact that multifrequency studies of ram-pressure-stripped galaxies reveal a spectral index decline with distance (Vollmer et al. 2013; Müller et al. 2021; Roberts et al. 2022b; Ignesti et al. 2022c), suggesting that the timescale of synchrotron loss is shorter than that of adiabatic loss. Under these conditions, the synchrotron emissivity spectrum $j(\nu/\nu_{\rm br})$ is defined as

$$j\left(\frac{\nu}{\nu_{\rm br}}\right) = \sqrt{3}\frac{e^3}{m_{\rm e}c^2} \int_0^{\frac{\pi}{2}} \sin^2\theta {\rm d}\theta \int_0^{+\infty} n(\gamma) F\left(\frac{\nu}{\nu_{\rm br}}\right) {\rm d}\gamma, \quad (2)$$

where θ is the pitch angle, $\nu_{\rm br} = \frac{3}{2}\frac{eB\sin\theta}{m_{\rm e}c}\gamma^2$ is the break frequency, $F(\nu/\nu_{\rm br})$ is the synchrotron kernel function (Rybicki & Lightman 1979), e and $m_{\rm e}$ are the electron charge and mass, respectively, and $n(\gamma) \propto \gamma^{\delta}$ is the CRe energy distribution. We compute a sampled spectrum for $j(\nu/\nu_{\rm br})$ by numerically solving Eq. (2) under the assumption of $\delta = -2.2$, which entails an injection index of $\alpha = (\delta+1)/2 = -0.6$, and a favorable minimal-energy-loss magnetic field of $B = B_{\rm CMB}/\sqrt{3} \simeq 2.2\,\mu$G, where $B_{\rm CMB} = 3.25(1+z)^2 \simeq 3.8\,\mu$G is the CMB equivalent magnetic field. The latter implies that we are assuming the maximum CRe radiative time. The implications of our assumptions are discussed in Sect. 4.3.

In order to associate the emissivity spectrum to the observed flux density profiles, it is necessary to assume a "bulk velocity" for the radio plasma along the stripping direction. The velocity defines the "dynamic age" of the radio plasma, which is the time elapsed since it left the stellar disk. For simplicity, we assume that the radio plasma moves with a uniform velocity V along the stripping direction, and that it leaves the stellar disk immediately after being injected into the ISM. Consequently, the time elapsed since the CRe injection can be estimated as $\tau = D/V$, where D is the (projected) distance from the stellar disk, and V is the (projected) CRe bulk velocity with respect to the galaxy. We note that both D and V are projected quantities, but their ratio is equivalent to the ratio of the deprojected values. Therefore, the observed projected distances can be associated with a corresponding τ. Then, to derive the corresponding model emissivity, we make use of the following radiative time definition to compute the corresponding $t_{\rm rad}$:

$$t_{\rm rad} \simeq 3.2 \times 10^{10} \frac{B^{1/2}}{B^2 + B_{\rm CMB}^2} \frac{1}{\sqrt{\nu_{\rm br}(1+z)}}\ {\rm yr}, \quad (3)$$

where the magnetic fields are expressed in μG and the observed frequency $\nu_{\rm br}$ is in units of MHz (Miley 1980). Under the assumption that the radiative age of the plasma coincides with the time elapsed since the injection, that is, $t_{\rm rad} \simeq \tau = D/V$, for a given V, Eq. (3) associates to each spatial bin a corresponding $\nu_{\rm br}(D)$ that in turn defines a value of $\nu/\nu_{\rm br}(D)$ for a given ν. Finally, we compute the emissivity by interpolating the corresponding $j(\nu/\nu_{\rm br}(D))$ from the sampled emissivity spectrum

Table 2. Sample of galaxies studied in this work.

ID	Name	RA, Dec [°, °]	z	R_{CL} [kpc]
1	LEDA 2667121	257.823, 64.342	0.0768	1781.66
2	LEDA 3138983	258.141, 64.098	0.0762	259.13
3	[PVK2003] 258.09561+64.14133	258.095, 64.141	0.0752	514.6
4	[YZJ2003] 2–63	258.334, 64.009	0.0799	406.32
5	LEDA 59848	258.213, 64.073	0.0738	55.93
6	[YZJ2003] 2–130	257.894, 63.894	0.0767	1198.62
7	LEDA 2665175	257.914, 64.169	0.0768	920.2

Notes. From left to right: identification number used in this paper; galaxy ID; Coordinates of the first sampling bin; SDSS redshift; projected clustercentric distance.

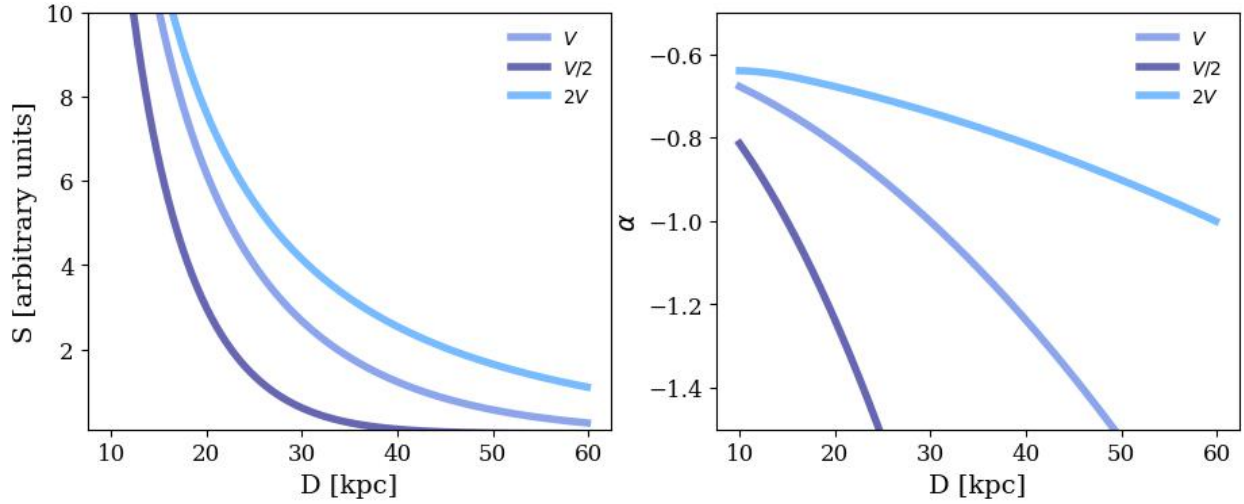

Fig. 2. Flux density (left) and spectral index (right) model profiles for different values of the velocity V given a magnetic field B_{min}.

derived from Eq. (2). We also introduce a normalization factor A that incorporates the conversion from emissivity to observed flux density. This procedure provides us with a flux density model profile as a function of the distance, which we can use to fit the observed flux density profiles to constrain V. By combining the interpolated emissivity values for two different frequencies at each distance, Eq. (1) permits us to also model the expected spectral index profile $\alpha(D)$, which we used to fit the observed spectral indexes. In general, this model predicts that flux density decreases monotonically with distance, with a consequent spectral index steepening. The trend is tuned by the velocity, where the lower (higher) the value of V, the steeper (flatter) the resulting profiles. As a consequence of our assumption of $\delta = -2.2$, the flattest spectral index value allowed by this model is $\alpha = -0.6$. For reference, we show in Fig. 2 how the resulting flux density and spectral index profiles change for different values of V for a fixed $B = B_{min}$.

We use a least-square fit to constrain the two free parameters, V and A, which are used to adapt our sampled model profiles to the observed ones. Briefly, the former tunes the model steepening along the x-axis, whereas the latter matches model and observations along the y-axis. For each galaxy, we fit the 144, 400 MHz flux density, and spectral index profiles independently to see whether or not the model can infer consistent velocities. We take into account both the uncertainties for the flux density and spectral index to compute the error on the velocity and the 1σ confidence interval for the best-fitting model.

3. Results

Figure 3 shows the sampling grid super-imposed on the SDSS image and the 144 MHz (blue) and 400 MHz (red) contours, the corresponding flux density, and spectral index profiles, and the best-fit with the computed values of V, for each of the seven galaxies of our sample. The results are summarized in Table 3 and Fig. 4. Due to the low number of bins of some galaxies, the best-fit uncertainties cannot be computed for every system.

Concerning the observed profiles, we note that, in general, every galaxy shows a decreasing flux density profile at both frequencies. The 400 MHz profiles are systematically shorter than the 144 MHz one, which is consistent with the fact that the CRe emitting at higher frequency in a uniform magnetic field have shorter radiative times than those emitting at lower frequencies (Eq. (3)). This means the CRe emitting at higher frequencies are not able to travel as far as those emitting at lower frequencies. The spectral index profiles seem to steepen with distance in four out of seven galaxies.

Regarding the model fitting, we observe that, although the 144 MHz profiles have a higher number of bins than the 400 MHz one and should therefore result in more robust results, the 400 MHz fit tends to have smaller uncertainties. We conclude that this is due to the fact that the curvature of the 400 MHz profile is more evident than that of the 144 MHz profiles, thus simplifying the fit convergence. The outcomes of the model fitting are varied:

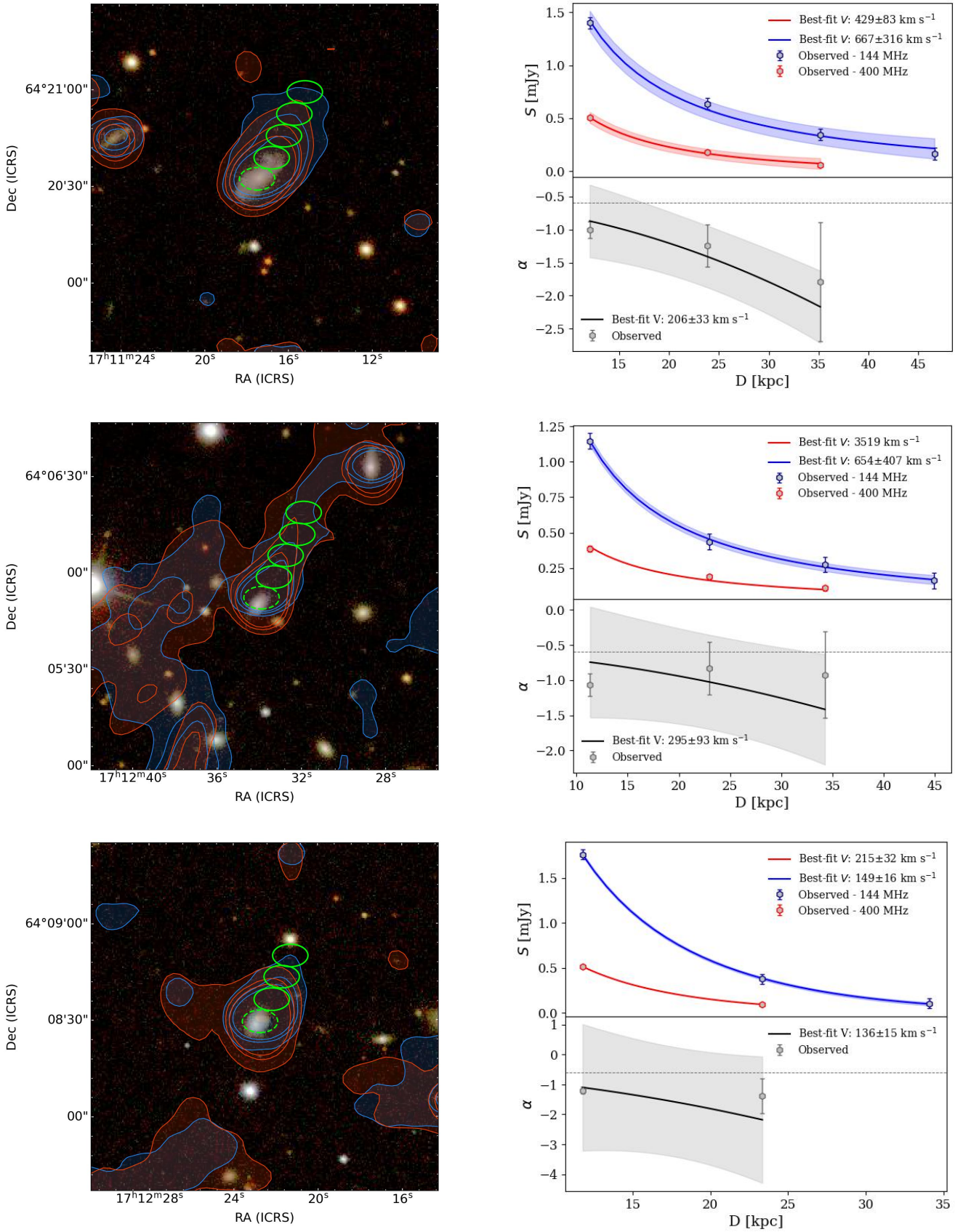

Fig. 3. Velocity fits for galaxies #1, #2, and #3 (from top to bottom). Left: SDSS RGB image overlapped with the 3, 9, 15×rms surface brightness contours at 144 (blue) and 400 MHz (orange) and the sampling regions (green ellipses). The dashed region marks the reference center of the galaxy. Right: flux density (top) and spectral index (bottom) trends with the distance from the stellar disk, and the corresponding best-fit profiles. The color-filled area indicates the 1σ confidence region. The horizontal dashed line indicates $\alpha = -0.6$.

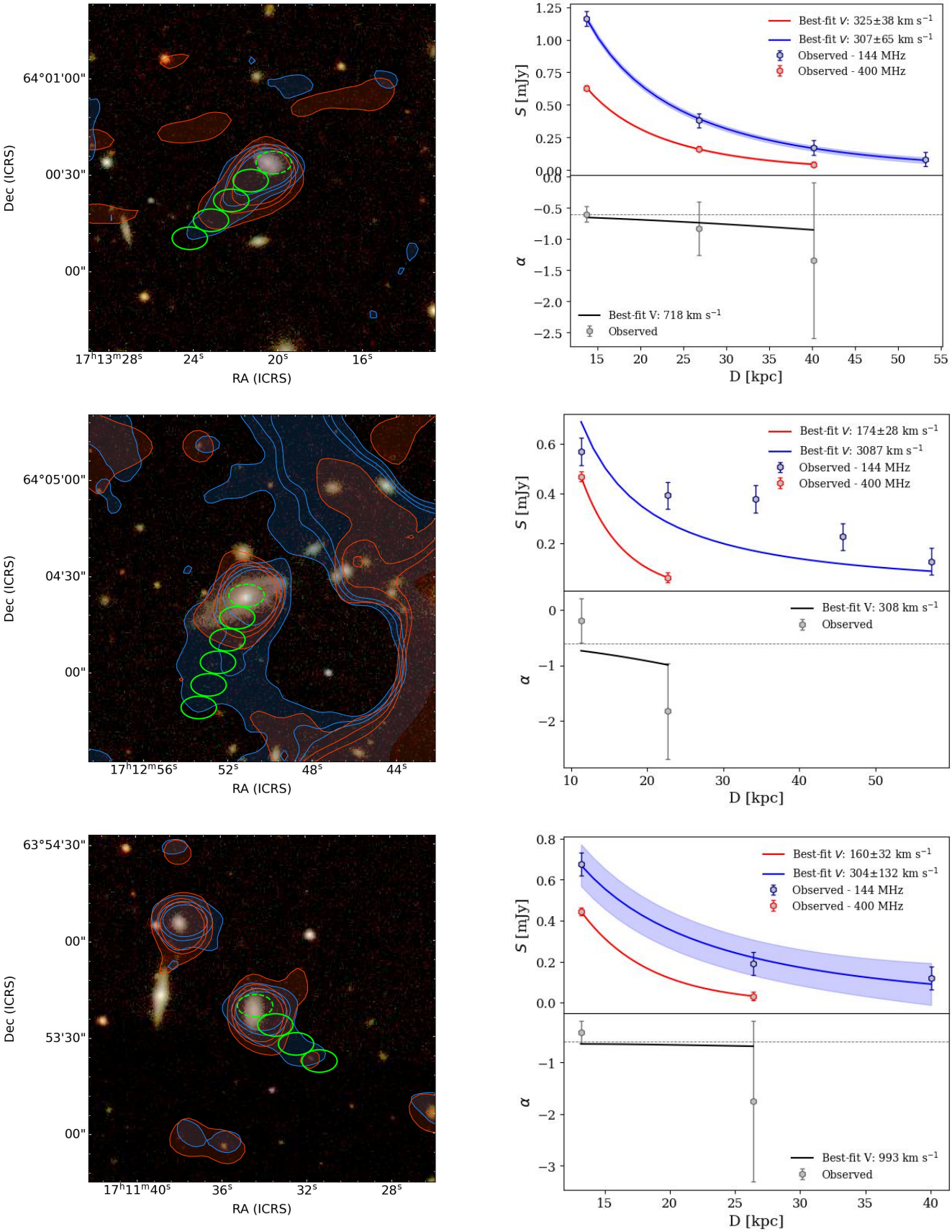

Fig. 3. continued. Velocity fit for galaxies #4, #5, and #6 (from top to bottom).

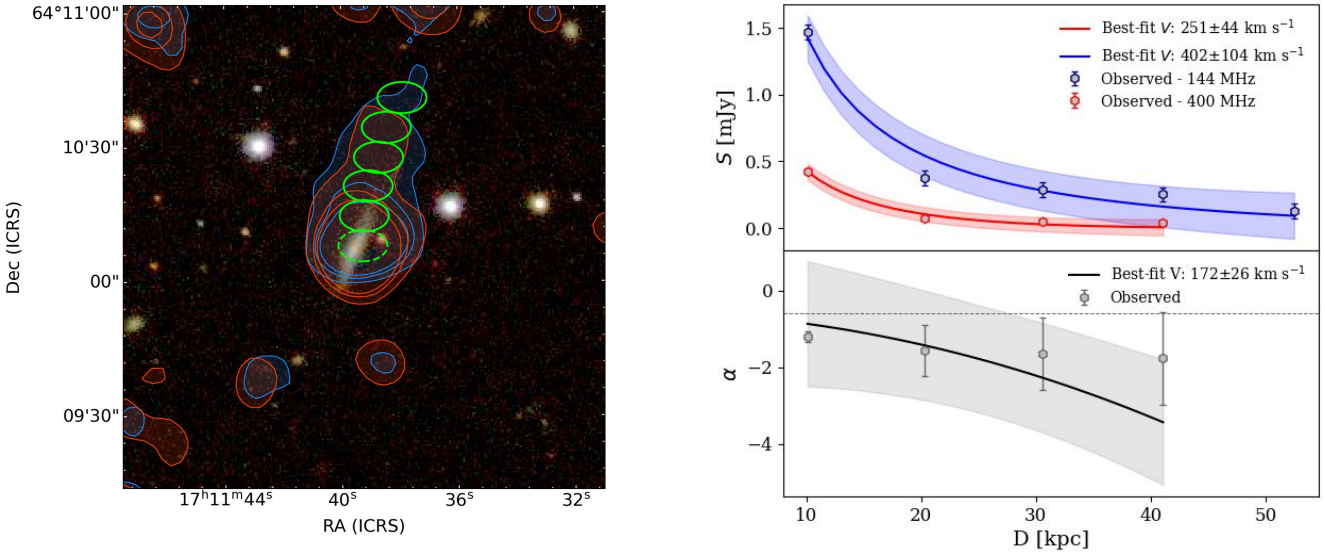

Fig. 3. continued. Velocity fit for galaxy #7.

Table 3. Best-fitting velocities in units of km s^{-1} derived from the different profiles and the 1σ uncertainties for the systems with sufficient statistics.

ID	V_{144}	V_{400}	V_α
1	667 ± 316	429 ± 83	206 ± 33
2	654 ± 407	3519	295 ± 93
3	149 ± 16	215 ± 32	136 ± 15
4	307 ± 65	325 ± 38	718
5	3087	174 ± 28	718
6	304 ± 132	160 ± 32	993
7	402 ± 104	251 ± 44	172 ± 26

- For galaxies #1, #3, and #7, the velocities derived from the three tracers are consistent within 2σ.
- For galaxies #4 and #6, the results are less clear. On the one hand, the flux density fit produces consistent results for the 144 and 400 MHz profiles. On the other hand, the spectral index fitting does not converge due to the fact that the values in the first bins are flatter than −0.6, which is the upper limit permitted by our model. A spectral index with such a flat value suggests that, inside those bins, the radio emission at 144 MHz either has an injection index of flatter than −0.6, or that it has been affected by ionization losses, which are not included in our simple model. Nevertheless, the spectral index profiles steepen with the distance, which is in agreement with our predictions.
- For galaxies #2 and #5, our results are inconclusive because either the flux densities or the spectral index profiles are not decreasing monotonically. In both cases, we conclude that this is because the radio tails are not real and/or are induced by the RPS. For galaxy #2, we suggest that the putative radio tail is instead the result of a blend of the emission from two galaxies due to the insufficient resolution of our images. For galaxy #5, we conclude that the "tail" is actually mostly composed of emission coming from the relatively close, bright radio galaxy. Consequently, the fit could not converge and it returns nonphysical and inconsistent values of V. Therefore, we exclude these two galaxies from the following discussion.

4. Discussion

4.1. Insights into the properties of the stripped tails

4.1.1. The life cycle of the radio plasma

The semi-empirical model introduced in Sect. 2.3.2 reproduces the profiles of five of the seven radio tails in A2255. This allows us to investigate the physical properties of the radio-emitting CRe and the stripped ISM. To begin with, the best-fit velocities are of the order of hundreds of km s^{-1} (see Table 3). These values support previous results that constrained the CRe bulk velocity to be of the order of the ram pressure winds (Ignesti et al. 2022c). Our semi-empirical model provides an accurate measure of the CRe bulk velocity in these extraplanar fields, which can be used to constrain numerical simulations of the nonthermal ISM components subjected to ram pressure (e.g., Tonnesen & Stone 2014; Müller et al. 2021; Farber et al. 2022).

Concerning the radio plasma properties, in general we observe that the flux density and spectral index profiles decline monotonically with distance, in agreement with the simple, pure cooling model. The emerging picture is that the radio plasma stripped from the stellar disk can cool down within the first tens of kpc via synchrotron emission before being dissipated by adiabatic expansion or mixing with the ICM. This confirms that the adiabatic loss timescale t_{ad} is longer than the CRe radiative time t_{rad} at 144 MHz, which allows us to propose a tentative constraint on t_{ad} of >100 Myr (Eq. (3)).

The observed profiles can constrain the action of "re-energization" processes that would induce deviations from the monotonic decline. These include star formation taking place outside of the stellar disk, and (re-)acceleration processes induced by shocks and turbulence within the tail. The former is expected to interfere with the cooling by injecting fresh electrons along the tail, forming a "bump" in the flux density profile and a flattening in the spectral index profile (e.g., the case of JO206; see Müller et al. 2021). In our sample, only galaxy #7 shows a potential signature of this process for $D > 30$ kpc, beyond which the observations slightly diverge from the model. This feature could either be a signature the presence of "fresh" CRe produced in situ by extraplanar star formation, or may suggest that the CRe losses are dominated by adiabatic losses instead of synchrotron or IC (e.g., due to increasingly long radiative times

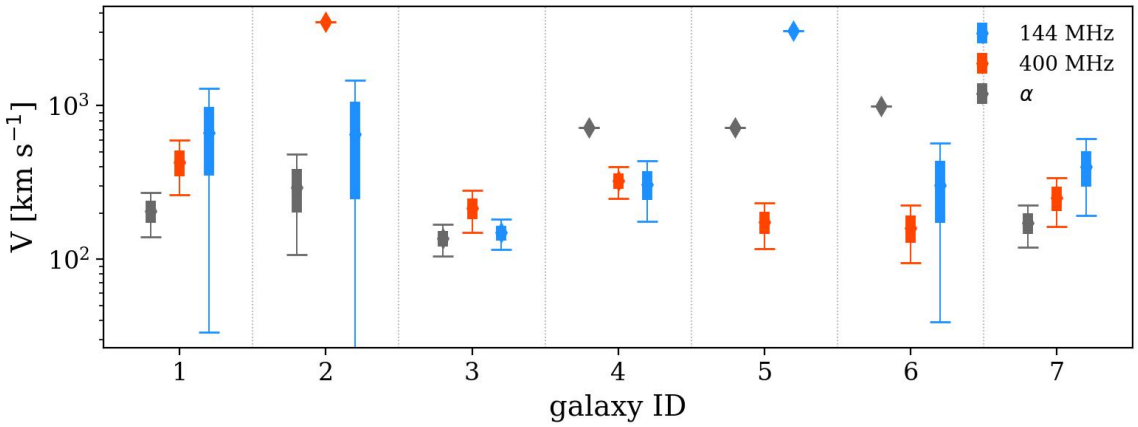

Fig. 4. Best-fitting V for each galaxy measured from the 144 (blue), 400 MHz (red), and spectral index (gray) profiles. The thick and thin error bars represent, respectively, the 1 and 2σ confidence intervals.

as a consequence of a decrease in the magnetic field with distance). However, we note that not observing a clear bump for the other galaxies does not rule out the possibility of star formation in the stripped tail. It may be possible that the signal due to the supernovae exploding in the tail is simply overcome by the signal of the CRe coming from the disk (see Ignesti et al. 2022a,b). In order to rule out the presence of extra-planar star formation, future optical and UV studies of the stripped tails are required (e.g., Poggianti et al. 2019b; Giunchi et al. 2023; Waldron et al. 2023). On the other hand, the CRe re-acceleration, by extending the lifetime of the CRe beyond their supposed radiative time (Eq. (3)), should act on the flux density profile by extending it with an additional component with a characteristic uniform surface brightness. These re-accelerated tails are being observed increasingly frequently in radio galaxies thanks to LOFAR, and have been explained as the consequence of the CRe being "gently re-accelerated" by the ICM turbulence for $t > t_{\rm acc}$, where $\tau_{\rm acc} > 100$ Myr is the re-acceleration timescale (e.g., de Gasperin et al. 2017; Botteon et al. 2021; Ignesti et al. 2022c; Edler et al. 2022). Consequently, not observing low-brightness tails in these star-forming galaxies may imply that the re-acceleration is not efficient enough to compensate for the energy losses, which are either due to synchrotron losses at 144 MHz or adiabatic expansion of the relativistic plasma (i.e., $t_{\rm rad} < t_{\rm ad} < t_{\rm acc}$). These broad constraints might suggest that, for those CRe emitting at 144 MHz, $t_{\rm rad} < 100$ Myr, and therefore, according to Eq. (3), the magnetic field is at least $\sim$7 μG.

4.1.2. Implications for the stripped ISM

Our results can provide constraints on the velocity of the stripped material due to RPS and can therefore help in the study of the evolution of the stripped clouds outside of the stellar disks (e.g., Sparre et al. 2020; Tonnesen & Bryan 2021; Farber et al. 2022). Although the order of magnitude is consistent with the previous numerical simulations, these latter predict that the cloud should decelerate as a consequence of the mixing with the ICM within $\sim$100 kpc from the disk (e.g., Tonnesen & Bryan 2021, and references therein). In this context, our model shows that the average velocity of the clouds within the first tens of kpc is relatively constant, and therefore the ICM mixing and the consequent deceleration have not yet significantly affected the clouds. Similarly, the observed spectral steepening indicates that, at least within the first tens of kpc from the stellar disk, the radio plasma can cool down undisturbed. This implies that the radiative time is shorter than the timescales of those processes that would eventually lead to the destruction of the stripped clouds, such as adiabatic expansion or mixing. Therefore, this piece of evidence tentatively constrains the order of magnitude of the lifetime of the stripped ISM clouds outside of the disk to be at least of the order of tens of millions of years.

4.2. A potential constraint on the 3D galaxy motion

In the RPS framework, the radio plasma and the ISM are being displaced by the ram pressure wind. Consequently, the stripped plasma bulk velocity, at least within the first tens of kpc from the disk, should be comparable with the galaxy velocity with respect to the ICM. The observed flux density profile of a radio tail should keep track of this information, and so we speculate that the velocity estimated by our model can be used to constrain the galaxy velocity in the cluster. Specifically, the modulus of the projected velocity V would represent a lower limit[2] on the projected galaxy velocity $V_{\rm sky}$ at which the galaxy is moving with respect to the ICM along the plane of the sky. The velocity component along the line of sight can be derived from the galaxy redshift z by following the method described in Davis & Scrimgeour (2014) to compute the peculiar velocities:

$$V_{\rm los} = c\left(\frac{z - z_{\rm cl}}{1 + z_{\rm cl}}\right). \quad (4)$$

Therefore, the galaxy total 3D velocity would be $V_{\rm tot} = \sqrt{V_{\rm sky}^2 + V_{\rm los}^2}$. Following this approach, we estimate the 3D velocity of the galaxies by adopting the velocity measured at 400 MHz as $V_{\rm sky}$. The resulting total velocities, which are summarized in Table 4, span from 1 to 2×$\sigma_{\rm cl}$. The 3D velocities, with the sole exception of galaxy #3, seem to be dominated by the line-of-sight velocity. As a proof of concept, in the following we explore the potential of using the CRe bulk velocity as an indicator of the galaxy velocity along the plane of the sky.

4.2.1. Comparing different estimators of $V_{\rm sky}$

First, we compare the velocity inferred from the radio properties of the tails with that derived using other, previously adopted methods in the literature. The results of this comparison should be interpreted with caution given the small size of our sample,

[2] Due to our assumptions on the magnetic field; see Sect. 2.3.2.

Table 4. Parameters describing the galaxies motion in the cluster as inferred from our analysis.

ID	V_{sky} [km s^{-1}]	V_{los} [km s^{-1}]	V_{tot} [km s^{-1}]	n_e [$\times 10^{-3}$ cm^{-3}]	P_{Ram} [$\times 10^{-11}$ erg cm^{-3}]
1	429 ± 83	–935	1029 ± 34	0.07 ± 0.01	0.14 ± 0.01
3	215 ± 32	–1355	1372 ± 5	0.81 ± 0.03	2.91 ± 0.1
4	325 ± 38	–64	331 ± 37	0.99 ± 0.04	0.21 ± 0.05
6	160 ± 32	–961	975 ± 5	0.19 ± 0.01	0.34 ± 0.01
7	251 ± 44	–928	962 ± 11	0.31 ± 0.01	0.56 ± 0.02

Notes. From left to right: Galaxy ID (see Table 2); best-fit V_{sky}; V_{los} derived from galaxy redshift (see Table 2); total velocity computed as $V_{tot} = \sqrt{V_{sky}^2 + V_{los}^2}$; electron density at the projected clustercentric distance (Fig. 6); ram pressure computed as $P_{Ram} = 1.19 \mu m_p n_e V_{tot}^2$.

and the fact that they are all part of the same cluster. Nevertheless, this exercise can provide a means to better evaluate the limits of each method in future studies. The two most frequently used methods are as follows:

- The 45° approximation: observing RPS-induced tails –at any wavelength– is evidence that the galaxy has a significant component of its velocity directed along the plane of the sky. Therefore, at the zeroth-order approximation, we can assume that V_{sky} is at least equal to V_{los}, and therefore $V_{tot} = V_{los}\sqrt{2}$. This is equivalent to assuming that the galaxy motion is inclined by 45° with respect to the line of sight. This method has been adopted to constrain the order of magnitude of the ram pressure given the ICM density (e.g., Poggianti et al. 2019a; Campitiello et al. 2021; Bartolini et al. 2022).
- The cooling length: this method is based on the same physical assumption as our work, that is, that the length of the radio tail depends solely on the CRe bulk velocity and the radiative time. However, in this case, the hypothesis is that the CRe emit all of their energy within the observed radio tail. The average CRe velocity, V_{avg}, is directly computed as the ratio between the total length of the radio tail and the radiative time. This method was typically applied when the radio data did not allow a detailed sampling of the flux density decline (Ignesti et al. 2022b; Müller et al. 2021). The most important caveat to using this method is that the resulting velocity mostly depends on the observed (projected) tail length, which ultimately depends on the image sensitivity.

We compute V_{sky} for each galaxy by adopting the two methods described above. For the latter one, we use the distance of the last bin of each galaxy as a measure of the radio length, and a $t_{rad} \simeq 2\times10^8$ yr derived from Eq. (3) under the same assumptions of our fit ($B = B_{min}$, $z = 0.08012$, and $\nu = 144$ MHz). The results are shown in Fig. 5, where, for each galaxy, we report the three different estimates of V_{sky} (bottom row, diamonds), and the corresponding V_{tot} (upper row, hexagons).

Of the three methods, the cooling length method generally produces the lowest values of V_{sky}, with the only exception being galaxy #3 for which $V_{avg} \simeq V$. This result suggests that assuming the CRe have exhausted their energy within the observed length may not be correct, and not taking into account the intrinsic curvature of the radio emissivity with time (distance) leads to underestimation of V_{sky} by a factor of ≤3 because of the nonlinearity of the $t_{rad}-\nu$ (and therefore $t_{rad}-D$) relation. Concerning the other method, the results are varied. For galaxy #4, the V_{los} is extremely low (64 km s^{-1}), suggesting that using the 45° approximation may have lead to underestimation of the velocity. In this case, the independent estimate provided by the radio emission allows us to obtain a more realistic constraint on the velocity. In the other galaxies, the velocity estimates are more similar. As

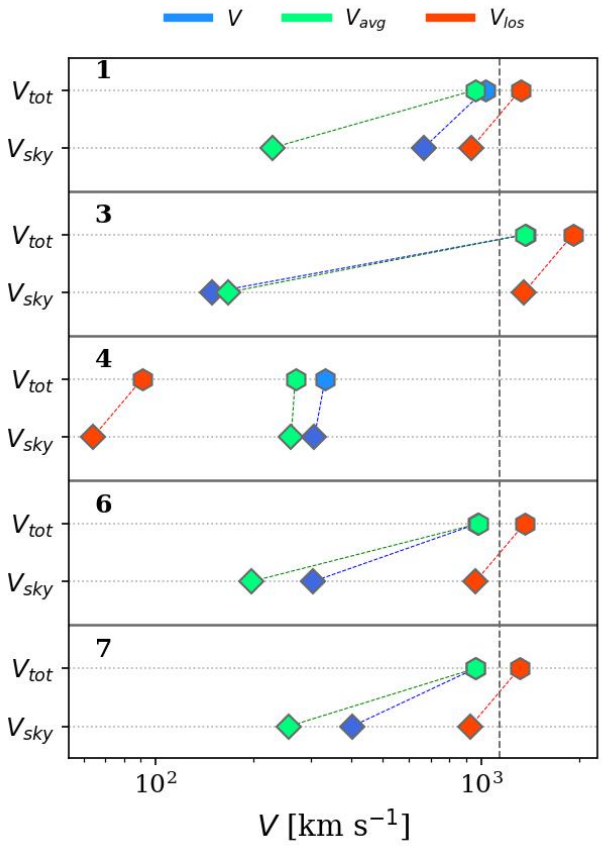

Fig. 5. Comparison between the v_{sky} derived with three different methods for each of the galaxies of our sample (lower row, diamonds) and the corresponding total velocities (upper row, hexagons), connected by the dashed lines. The three methods are: the best-fit velocity V derived from the 400 MHz profile (blue), $v_{sky} = v_{los}$ (red), and $v_{sky} = v_{avg}$ (green). The vertical dashed line shows the value of σ_{cl}.

mentioned above, this could be a result of the sample bias due to the physical properties of the cluster and the galaxies within. On the other hand, although the results are similar, computing the velocity on the basis of the radio emission decline permits us to also investigate the geometry of the galaxy–wind interaction (see Sect. 4.2.3), which is not possible otherwise. This methodology therefore confers a certain advantage with respect to the 45° approximation.

4.2.2. Measuring the effective ram pressure

Given the galaxy velocity and position in the cluster, the corresponding ICM ram pressure can be computed as $P_{Ram} =$

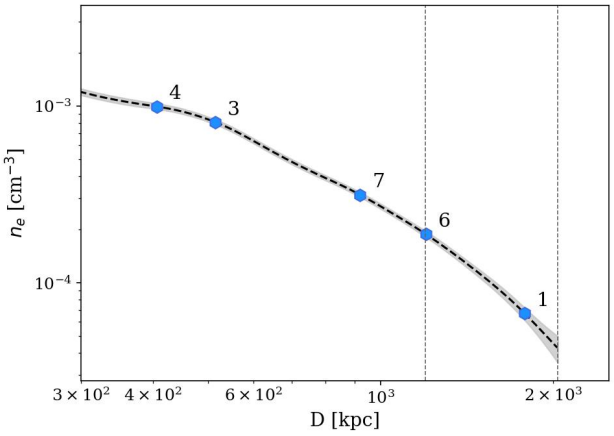

Fig. 6. Electron density profile reported in X-COP. The blue points mark the galaxy positions, and the vertical dashed lines indicate R_{500} and R_{200}, from left to right.

$\rho_{\rm ICM} V_{\rm tot}^2$, where $\rho_{\rm ICM} = 1.19 \mu m_{\rm p} n_{\rm e}$ and μ, $m_{\rm p}$, and $n_{\rm e}$ are, respectively, the average molecular weight, the proton mass, and the electron density (e.g., Gitti et al. 2012). To compute the latter, we use the azimuthally averaged electron density profile[3] measured by the X-COP survey (Ghirardini et al. 2019) to evaluate the proper $n_{\rm e}$ at the projected clustercentric distance of each galaxy (Fig. 6). The corresponding uncertainties are derived by propagating the error on the fit and the uncertainty on $n_{\rm e}$. We report the results in Table 4. The caveats, limitations, and assumptions of this method are discussed in Sect. 4.3. In general, the resulting values of $P_{\rm Ram}$ lie in the 10^{-12}–10^{-11} erg cm^{-3} range, which is in line with the previous predictions (Roediger & Hensler 2005; Brüggen & De Lucia 2008; Jaffé et al. 2018; Boselli et al. 2022).

4.2.3. Computing the disk–wind angle

Measuring the two components of the 3D velocity independently allows us to constrain the inclination of the galaxy disk with respect to the direction of its motion, which corresponds to the geometry of the ram pressure wind with respect to the stellar disk. Indeed, several studies have shown that the evolution of ram-pressure-stripped galaxies can be affected by the inclination of the ram pressure wind, which is opposite to the galaxy motion, and the stellar disk (e.g., Roediger & Brüggen 2006; Jáchym et al. 2009; Bekki 2014; Steinhauser et al. 2016; Farber et al. 2022; Akerman et al. 2023). The disk–wind angle has previously been derived for individual galaxies (e.g., Vollmer et al. 2012; Merluzzi et al. 2013). Here, we derive the disk–wind angles for the five galaxies for which the semi-empirical model introduced in Sect. 2.3.2 reproduces the profiles of radio tails; we do this in order to increase the number of systems with this crucial information, and to demonstrate our geometrical model, which takes advantage of the results of our radio analysis.

We compute the disk–wind angle, Θ, starting from our estimates of $V_{\rm sky}$ and $V_{\rm los}$. We adopt a reference system in which the x- and y-axes are on the plane of the sky along the east–west and the north–south directions, respectively, and the z-axis coincides with the line of sight and points towards the observer. For each galaxy, we use the inclination of the stellar disk with respect to the line of sight, $\phi_{\rm disk}$, and its position angle, PA, reported in the HyperLeda[4] database (Makarov et al. 2014). With them, we define the polar versor $\hat{n}$ in a cartesian coordinate system centered on the galaxy with the three components aligned along the directions north–south, east–west, and the line of sight, respectively (Fig. 7). Similarly, with $V_{\rm sky}$ and $V_{\rm los}$, where $V_{\rm los} > 0$

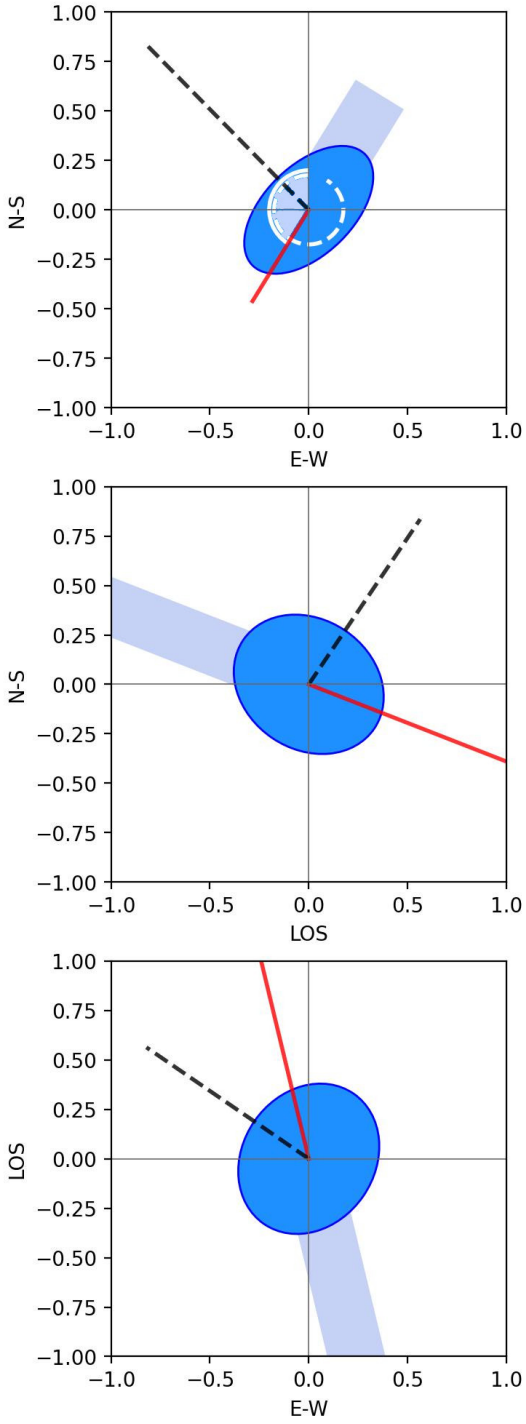

Fig. 7. Example of the 3D projections in the cartesian system for galaxy #1. The blue disk and segment represent the stellar disk and the observed radio tail. The red and black vectors are, respectively, the projections of $\hat{v}$ and $\hat{n}$. From top to bottom: projection along the LOS (which corresponds to the observed projection), along the E–W axis, and along the N–S axis. In the top panel, we show the θ_V (white, filled) and the $\theta_{\rm tail}$ (white, dashed) angles.

[3] https://dominiqueeckert.wixsite.com/xcop/a2255

[4] http://leda.univ-lyon1.fr/

Table 5. Angles describing the galaxy motion and the disk–wind interaction.

ID	$\theta_{\rm tail}$	$\phi_{\rm disk}$	PA	Θ	ϕ_V
1	328.38	64.3	134.5	76.85	35.5
3	333.69	52.1	153.1	52.43	6.27
4	131.22	41.5	58.6	39.45	78.2
6	227.18	55.8	178.5	43.68	17.55
7	351.0	90.0	154.2	96.6	23.43

Notes. From left to right: galaxy ID; north-to-east angle between the galaxy center and the tail direction in the sky; inclination and position angle as reported on HyperLeda; angle between the polar axis and the velocity versor; inclination of the velocity with respect to the line of sight. The values are in units of degrees.

indicates a galaxy moving away from the observer, and the direction of the motion, which we estimate as $\theta_V = \theta_{\rm tail} - \pi$ where $\theta_{\rm tail}$ is the north-to-east angle between the galaxy center and the direction of the tail in the sky, we define the velocity versor $\hat{v}$. Therefore,

$$\begin{aligned}\hat{n} =&[\cos(\mathrm{PA})\sin(\phi_{\rm disk}),\\ &\sin(\mathrm{PA})\sin(\phi_{\rm disk}),\\ &\cos(\phi_{\rm disk})]\\ \hat{v} =&[V_{\rm sky}\cos(\theta_V+\pi/2),\\ &V_{\rm sky}\sin(\theta_V+\pi/2),\\ &-V_{\rm los}]/V_{\rm tot}.\end{aligned} \tag{5}$$

The disk–wind angle can then be computed as the angle between $\hat{v}$ and $\hat{n}$, and therefore

$$\Theta = \arccos(\hat{v}\cdot\hat{n})\cdot \tag{6}$$

In this reference system, $\Theta = 90$ indicates a wind impacting the galaxy edge-on, whereas $\Theta = 0$ or $\Theta = 180$ indicate that the galaxy is facing the wind face-on. We can also measure the inclination of the wind with respect to the line of sight, ϕ_V, as

$$\phi_V = \arctan\left(\frac{V_{\rm sky}}{V_{\rm los}}\right)\cdot \tag{7}$$

We report the results for each galaxy in Table 5.

We compare the values of ϕ_V inferred by our analysis with those derived from an independent method, namely the phase-space analysis presented in Sect. 3 of Bellhouse et al. (2021). The probable angle of a galaxy's velocity between the line of sight and the plane of the sky is estimated by comparing the observed $R_{\rm CL}/R_{200}$ and $V_{\rm los}/\sigma_{\rm cl}$ with a phases-space diagram constructed by stacking the galaxies of 42 simulated galaxy clusters observed from random angles (e.g., Smith et al. 2022a,b; Canducci et al. 2022; Awad et al. 2023, for different applications of the phase-space analysis). This method provides us with a distribution of ϕ_V for each position in the phase-space diagram (i.e., for each couple of $R_{\rm CL}/R_{200}$ and $V_{\rm los}/\sigma_{\rm cl}$). Figure 8 shows the values of ϕ_V estimated by our analysis compared to the value range inferred from the phase-space analysis. We remind the reader that, due to our assumption on the magnetic field, we can derive only a lower limit for V, and therefore also for $V_{\rm sky}$. Correspondingly, the values of ϕ_V must be considered as lower limits for the real ϕ_V. For three galaxies, #1, #7, and #6, the two predictions are in broad agreement, in the sense that they lie in the same quadrant $\phi_V < 45°$, and for galaxies #1 and #7 they are indeed consistent. For galaxy #4, the phase-space prediction is consistent within the third quartile with $\phi_V > 45°$. Therefore, for three galaxies, and tentatively also for galaxy #4, the two independent analyses are in agreement. However, we note that the phase-space analysis is a statistical tool intended for large numbers of galaxies, and therefore this current comparison, albeit instructive, is not conclusive.

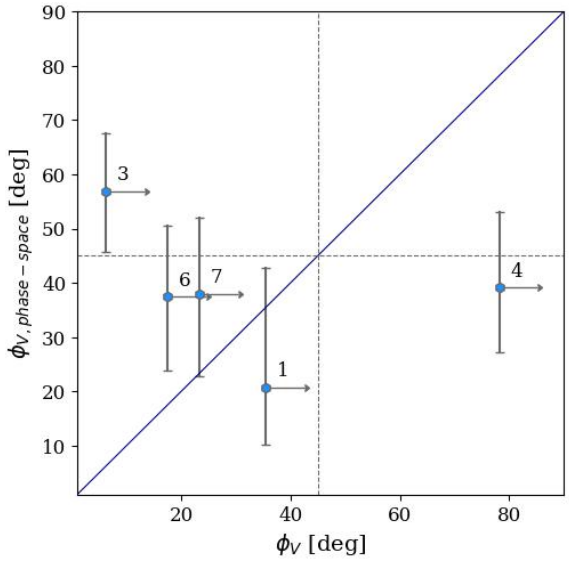

Fig. 8. Comparison between the values of ϕ inferred in our work (x-axis) vs. the prediction based on the phase-space analysis (y-axis). The vertical error bars indicate the first and third quartiles of the ϕ distributions predicted by the phase-space analysis. The dashed lines separate the two regimes $\phi_V > 45°$ ($V_{\rm sky} > V_{\rm los}$) and $\phi_V < 45°$ ($V_{\rm sky} < V_{\rm los}$), and the continuous line indicates the 1:1 identity.

4.3. Caveats

Below, we summarize the caveats, limitations, and assumptions of our model.

1. In order to obtain a reliable fit of the flux density decline, it would be best to sample the radio tails with at least three spatial bins, because the velocity fit is designed to constrain the curvature of the profile. This is only possible with radio images of the correct combination of sensitivity and resolution.

2. The best-fit V depends on the shape of the underlying emissivity spectrum, which ultimately depends on the assumptions on δ and B. Assuming a steeper CRe distribution than the one we adopt ($\delta = -2.2$) will produce a steeper initial spectral index than -0.6. In principle, the initial spectral index could be measured directly from the synchrotron spectrum within the stellar disk. However, in our case, this measure may not be reliable because a low-frequency spectral index in the presence of high-density star forming regions can be flattened by ionization losses and therefore does not reflect the real CRe energy distribution (e.g., Basu et al. 2015; Ignesti et al. 2022b). Concerning the magnetic field, because there are no methods to reliably measure its intensity in the tails, we assumed the minimal energy loss field $B_{\rm min}$. Assuming higher values of B would also result in a steeper emissivity decline for $\nu > \nu_{\rm br}$. The magnetic field assumption defines the conversion from radiative time to projected distance. Using $B_{\rm min}$ entails that we are working under the favorable hypothesis of maximum CRe radiative time, and therefore for a given velocity, we are maximizing the distance over which the CRe can travel. For this reason, the V (and therefore also $V_{\rm sky}$) derived under this assumption is a lower limit

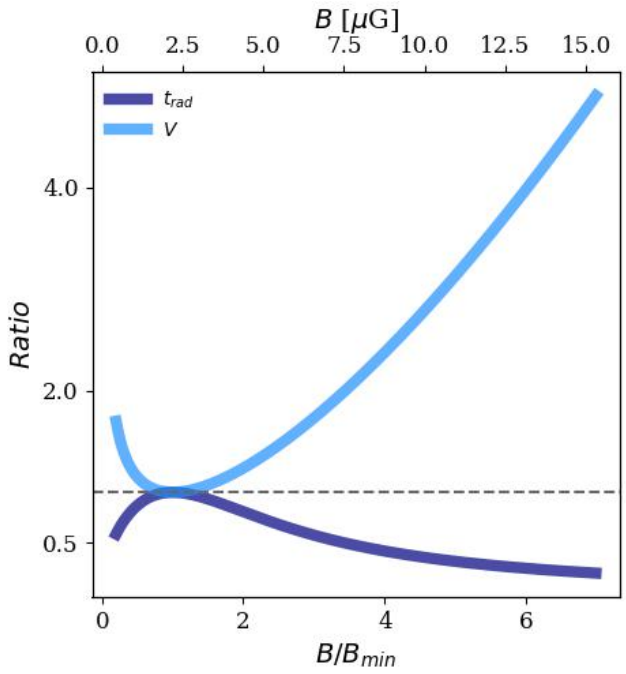

Fig. 9. Expected ratio of t_{rad} and V with respect to the case $B = B_{min}$ for different values of B/B_{min}.

on the real velocity. Using different values of B would entail shorter t_{rad} (Eq. (3)), and therefore higher velocities are required to reproduce the observed projected distances. We quantify this behavior in Fig. 9, in which we show how t_{rad} (dark blue) and $V_{sky} \propto 1/t_{rad}$ (light blue) change with respect to the case where $B = B_{min}$ for different values of B/B_{min}. We observe that the resulting V_{sky} exceeds the minimal energy loss estimate by a factor 2 for $B \geq 3.5 \times B_{min} \simeq 7.7\,\mu$G.

3. We assume that B and the CRe bulk velocity V are uniform along the tail. Different conditions would divert the observed flux density profiles from the prediction of pure synchrotron cooling. For instance, a magnetic field decreasing along the tail (e.g., as a consequence of adiabatic expansion) could entail a lower synchrotron emissivity, but may also imply that, at a given frequency, the emission would be provided by CRe with increasing energy, and therefore lower radiative times. Moreover, we assume that the CRe velocity along the tail is defined by the wind velocity, and therefore we neglected the possible effect of the CRe stream along the magnetic field lines (e.g., Armillotta et al. 2022).

4. By fitting the emissivity spectrum directly to the observed flux density, we are also inherently assuming that, in each bin, the radio-emitting plasma has the same geometrical properties, such as the volume, the curvature along the line of sight, and the filling factor. A decreasing volume or filling factor would induce an additional decline in flux density that is not included by our model.

5. The exact ram pressure, P_{Ram}, is derived from the azimuthally averaged n_e profile (Fig. 6), which is computed under the assumption of a geometrically spherical ICM. To infer the appropriate n_e for each galaxy, we use their projected cluster-centric distance, which is a lower limit on their real distance. Moreover, the assumption of spherical geometry may not hold in a complex merging cluster such as A2255. Therefore, the values of n_e reported in Table 4 should be considered upper limits on the real densities, and therefore also on P_{Ram}.

5. Conclusions

In this work, we present a semi-empirical model to reproduce the multi-frequency radio emission of ram-pressure-stripped tails, and its application. In order to test the model, we investigate the properties of the radio tails of seven spiral galaxies in A2255. We combined LOFAR and uGMRT observations at 144 and 400 MHz to infer the radio properties within few tens of kpc from the stellar disk. We observe a monotonic decrease in flux density associated with a spectral steepening along the stripping direction. We then modeled the observed profiles with a semi-empirical model, where the radio plasma moves with a uniform velocity V along the stripping direction and cools down via synchrotron radiation. The model reproduces the observed profiles for five out of seven galaxies, and constrains the projected radio plasma velocity along the tail to values of the order of 100−500 km s^{-1}. This result confirms the qualitative scenario built up over the years in the literature, and provides the first estimate of the radio plasma bulk velocity. Moreover, observing a monotonic spectral steepening entails that, at least within the first ∼30 (projected) kpc from the stellar disk, the radiative time, which is of the order of ∼100 Myr, is shorter than the adiabatic loss timescale.

The order of magnitude of the best-fit velocity supports the idea that the radio plasma clouds are transported by the ram pressure winds. Therefore, we speculate that this approach, in conjunction with measurement of the CRe bulk velocity, can constrain the galaxy velocity along the plane of the sky and provide us with the first estimate of the 3D velocity of these galaxies. As a proof of concept, we estimate the total velocity of these galaxies with respect to the ICM to be between 300 and 1300 km s^{-1}. We also infer the angle between the stellar disk and the ram pressure, and constrain the corresponding ram pressure exerted by the ICM to be between 0.1 and 2.9×10^{-11} erg cm^{-13}. These results represent the first estimates of these quantities for cluster galaxies with this method, and could be used to constrain future studies of these systems.

The proposed model should now be tested and refined on a larger sample of RPS galaxies, and, if possible, using multi-frequency observations spanning a wider wavelength range. Tests would greatly benefit from independent estimates of the extraplanar magnetic field, potentially provided by polarimetry studies. Moreover, our results should be complemented by tailored numerical MHD simulations of RPS. The method presented in this manuscript can be used to expand the applications of radio observations of RPS galaxies, whose availability is destined to increase over the coming years with the advance of all-sky surveys. Combination with deep radio, X-ray, and optical observations will create the possibility to quantitatively characterize the RPS affecting galaxies in dense environments.

Acknowledgements. We thank the referee for the suggestions which improved the quality of the manuscript. This project has received funding from the European Research Council (ERC) under the European Union's Horizon 2020 research and innovation programme (grant agreement No. 833824). A.I. acknowledges the INAF founding program 'Ricerca Fondamentale 2022' (PI: A. Ignesti). This work is the fruit of the collaboration between GASP and the LOFAR Survey Key Project team ("MoU: Exploring the low-frequency side of jellyfish galaxies with LOFAR", PI: A. Ignesti). R.Jv.W. acknowledges support from the VIDI research programme with project number 639.042.729, which is financed by the Netherlands Organisation for Scientific Research (NWO). I.D.R. acknowledges support from the ERC Starting Grant Cluster Web 804208. K.R. acknowledges support from *Chandra* grant GO0-21112X. A.I. thanks the music of Vulfpeck for providing inspiration during the preparation of the draft. LOFAR (van Haarlem et al. 2013) is the Low Frequency Array designed and constructed by ASTRON. It has observing, data processing, and data storage facilities in several countries, which are owned by various parties (each with their own

funding sources), and that are collectively operated by the ILT foundation under a joint cientific policy. The ILT resources have benefited from the following recent major funding sources: CNRS-INSU, Observatoire de Paris and Université d'Orléans, France; BMBF, MIWF-NRW, MPG, Germany; Science Foundation Ireland (SFI), Department of Business, Enterprise and Innovation (DBEI), Ireland; NWO, The Netherlands; The Science and Technology Facilities Council, UK; Ministry of Science and Higher Education, Poland; The Istituto Nazionale di Astrofisica (INAF), Italy. This research made use of the Dutch national e-infrastructure with support of the SURF Cooperative (e-infra 180169) and the LOFAR e-infra group. The Jülich LOFAR Long Term Archive and the German LOFAR network are both coordinated and operated by the Jülich Supercomputing Centre (JSC), and computing resources on the supercomputer JUWELS at JSC were provided by the Gauss Centre for Supercomputing e.V. (grant CHTB00) through the John von Neumann Institute for Computing (NIC). This research made use of the University of Hertfordshire high-performance computing facility and the LOFAR-UK computing facility located at the University of Hertfordshire and supported by STFC [ST/P000096/1], and of the Italian LOFAR IT computing infrastructure supported and operated by INAF, and by the Physics Department of Turin university (under an agreement with Consorzio Interuniversitario per la Fisica Spaziale) at the C3S Supercomputing Centre, Italy. We thank the staff of the GMRT that made these bservations possible. GMRT is run by the National Centre for Radio Astrophysics of the Tata Institute of Fundamental Research. This research made use of Astropy, a community-developed core Python package for Astronomy (Astropy Collaboration 2013, 2018), and APLpy, an open-source plotting package for Python (Robitaille & Bressert 2012). This research has made use of the SIMBAD database, operated at CDS, Strasbourg, France (Wenger et al. 2000).

References

Abell, G. O. 1958, ApJS, 3, 211
Ahumada, R., Prieto, C. A., Almeida, A., et al. 2020, ApJS, 249, 3
Akerman, N., Tonnesen, S., Poggianti, B. M., Smith, R., & Marasco, A. 2023, ApJ, 948, 18
Armillotta, L., Ostriker, E. C., & Jiang, Y.-F. 2022, ApJ, 929, 170
Astropy Collaboration (Robitaille, T. P., et al.) 2013, A&A, 558, A33
Astropy Collaboration (Price-Whelan, A. M., et al.) 2018, AJ, 156, 123
Awad, P., Peletier, R., Canducci, M., et al. 2023, MNRAS, 520, 4517
Bartolini, C., Ignesti, A., Gitti, M., et al. 2022, ApJ, 936, 74
Basu, A., Beck, R., Schmidt, P., & Roy, S. 2015, MNRAS, 449, 3879
Bekki, K. 2014, MNRAS, 438, 444
Bellhouse, C., McGee, S. L., Smith, R., et al. 2021, MNRAS, 500, 1285
Blanton, E. L., Randall, S. W., Douglass, E. M., et al. 2009, ApJ, 697, L95
Boselli, A., Fossati, M., & Sun, M. 2022, A&ARv, 30, 3
Botteon, A., Brunetti, G., van Weeren, R. J., et al. 2020a, ApJ, 897, 93
Botteon, A., van Weeren, R. J., Brunetti, G., et al. 2020b, MNRAS, 499, L11
Botteon, A., Giacintucci, S., Gastaldello, F., et al. 2021, A&A, 649, A37
Botteon, A., van Weeren, R. J., Brunetti, G., et al. 2022, Sci. Adv., 8, eabq7623
Briggs, D. S., & Cornwell, T. J. 1994, IAU Symp., 158, 212
Brüggen, M., & De Lucia, G. 2008, MNRAS, 383, 1336
Campitiello, M. G., Ignesti, A., Gitti, M., et al. 2021, ApJ, 911, 144
Canducci, M., Awad, P., Taghribi, A., et al. 2022, Astron. Comput., 41, 100658
Chen, H., Sun, M., Yagi, M., et al. 2020, MNRAS, 496, 4654
Condon, J. J. 1992, ARA&A, 30, 575
Cortese, L., Catinella, B., & Smith, R. 2021, PASA, 38, e035
Davis, T. M., & Scrimgeour, M. I. 2014, MNRAS, 442, 1117
de Gasperin, F., Intema, H. T., Shimwell, T. W., et al. 2017, Sci. Adv., 3, e1701634
Di Gennaro, G., van Weeren, R. J., Cassano, R., et al. 2021, A&A, 654, A166
Dressler, A. 1980, ApJ, 236, 351
Dursi, L. J., & Pfrommer, C. 2008, ApJ, 677, 993
Ebeling, H., Ma, C.-J., & Barrett, E. 2014, ApJS, 211, 21
Eckert, D., Ettori, S., Pointecouteau, E., et al. 2017, Astron. Nachr., 338, 293
Edler, H. W., de Gasperin, F., Brunetti, G., et al. 2022, A&A, 666, A3
Farber, R. J., Ruszkowski, M., Tonnesen, S., & Holguin, F. 2022, MNRAS, 512, 5927
Fasano, G., Poggianti, B. M., Couch, W. J., et al. 2000, ApJ, 542, 673
Feretti, L., Boehringer, H., Giovannini, G., & Neumann, D. 1997, A&A, 317, 432
Franchetto, A., Tonnesen, S., Poggianti, B. M., et al. 2021, ApJ, 922, L6
Fumagalli, M., Fossati, M., Hau, G. K. T., et al. 2014, MNRAS, 445, 4335
Gavazzi, G., & Jaffe, W. 1987, A&A, 186, L1
Ghirardini, V., Eckert, D., Ettori, S., et al. 2019, A&A, 621, A41
Gitti, M., Brighenti, F., & McNamara, B. R. 2012, Adv. Astron., 2012, 950641
Giunchi, E., Gullieuszik, M., Poggianti, B. M., et al. 2023, ApJ, 949, 72
Golovich, N., Dawson, W. A., Wittman, D. M., et al. 2019, ApJ, 882, 69
Gunn, J. E., & Gott, J. R., III 1972, ApJ, 176, 1
Harris, D. E., Kapahi, V. K., & Ekers, R. D. 1980, A&AS, 39, 215
Ignesti, A., Vulcani, B., Poggianti, B. M., et al. 2022a, ApJ, 937, 58
Ignesti, A., Vulcani, B., Poggianti, B. M., et al. 2022b, ApJ, 924, 64
Ignesti, A., Brunetti, G., Shimwell, T., et al. 2022c, A&A, 659, A20
Intema, H. T., van der Tol, S., Cotton, W. D., et al. 2009, A&A, 501, 1185
Jáchym, P., Köppen, J., Palouš, J., & Combes, F. 2009, A&A, 500, 693
Jaffe, W. J., & Rudnick, L. 1979, ApJ, 233, 453
Jaffé, Y. L., Poggianti, B. M., Moretti, A., et al. 2018, MNRAS, 476, 4753
Kenney, J. D. P., van Gorkom, J. H., & Vollmer, B. 2004, AJ, 127, 3361
Kenney, J. D. P., Geha, M., Jáchym, P., et al. 2014, ApJ, 780, 119
Lal, D. V., Lyskova, N., Zhang, C., et al. 2022, ApJ, 934, 170
Longair, M. S. 2011, High Energy Astrophysics (Cambridge: Cambridge University Press)
Makarov, D., Prugniel, P., Terekhova, N., Courtois, H., & Vauglin, I. 2014, A&A, 570, A13
Merluzzi, P., Busarello, G., Dopita, M. A., et al. 2013, MNRAS, 429, 1747
Miley, G. 1980, ARA&A, 18, 165
Miller, N. A., & Owen, F. N. 2003, AJ, 125, 2427
Moretti, A., Paladino, R., Poggianti, B. M., et al. 2020, ApJ, 889, 9
Müller, A., Poggianti, B. M., Pfrommer, C., et al. 2021, Nat. Astron., 5, 159
Murphy, E. J., Kenney, J. D. P., Helou, G., Chung, A., & Howell, J. H. 2009, ApJ, 694, 1435
Offringa, A. R., & Smirnov, O. 2017, MNRAS, 471, 301
Offringa, A. R., McKinley, B., Hurley-Walker, N., et al. 2014, MNRAS, 444, 606
Pacholczyk, A. G. 1970, Radio Astrophysics. Nonthermal Processes in Galactic and Extragalactic Sources (San Francisco: Freeman)
Peluso, G., Vulcani, B., Poggianti, B. M., et al. 2022, ApJ, 927, 130
Pfrommer, C., & Dursi, L. J. 2010, Nat. Phys., 6, 520
Pizzo, R. F., & de Bruyn, A. G. 2009, A&A, 507, 639
Planck Collaboration XXVII. 2016, A&A, 594, A27
Poggianti, B. M., Fasano, G., Omizzolo, A., et al. 2016, AJ, 151, 78
Poggianti, B. M., Moretti, A., Gullieuszik, M., et al. 2017a, ApJ, 844, 48
Poggianti, B. M., Jaffé, Y. L., Moretti, A., et al. 2017b, Nature, 548, 304
Poggianti, B. M., Ignesti, A., Gitti, M., et al. 2019a, ApJ, 887, 155
Poggianti, B. M., Gullieuszik, M., Tonnesen, S., et al. 2019b, MNRAS, 482, 4466
Rasmussen, J., Ponman, T. J., & Mulchaey, J. S. 2006, MNRAS, 370, 453
Roberts, I. D., & Parker, L. C. 2020, MNRAS, 495, 554
Roberts, I. D., van Weeren, R. J., McGee, S. L., et al. 2021, A&A, 652, A153
Roberts, I. D., Lang, M., Trotsenko, D., et al. 2022a, ApJ, 941, 77
Roberts, I. D., van Weeren, R. J., Timmerman, R., et al. 2022b, A&A, 658, A44
Robitaille, T., & Bressert, E. 2012, Astrophysics Source Code Library [record ascl:1208.017]
Roediger, E., & Brüggen, M. 2006, MNRAS, 369, 567
Roediger, E., & Hensler, G. 2005, A&A, 433, 875
Ruszkowski, M., Brüggen, M., Lee, D., & Shin, M. S. 2014, ApJ, 784, 75
Rybicki, G. B., & Lightman, A. P. 1979, Radiative Processes in Astrophysics (New York: Wiley)
Schellenberger, G., Giacintucci, S., Lovisari, L., et al. 2022, ApJ, 925, 91
Shimwell, T. W., Röttgering, H. J. A., Best, P. N., et al. 2017, A&A, 598, A104
Shimwell, T. W., Tasse, C., Hardcastle, M. J., et al. 2019, A&A, 622, A1
Shimwell, T. W., Hardcastle, M. J., Tasse, C., et al. 2022, A&A, 659, A1
Smith, R. J., Lucey, J. R., Hammer, D., et al. 2010, MNRAS, 408, 1417
Smith, R., Shinn, J.-H., Tonnesen, S., et al. 2022a, ApJ, 934, 86
Smith, R., Calderón-Castillo, P., Shin, J., Raouf, M., & Ko, J. 2022b, AJ, 164, 95
Sparre, M., Pfrommer, C., & Ehlert, K. 2020, MNRAS, 499, 4261
Steinhauser, D., Schindler, S., & Springel, V. 2016, A&A, 591, A51
Sun, M., Ge, C., Luo, R., et al. 2021, Nat. Astron., 6, 270
Tonnesen, S., & Bryan, G. L. 2021, ApJ, 911, 68
Tonnesen, S., & Stone, J. 2014, ApJ, 795, 148
Tonnesen, S., Bryan, G. L., & van Gorkom, J. H. 2007, ApJ, 671, 1434
van Gorkom, J. H. 2004, in Clusters of Galaxies: Probes of Cosmological Structure and Galaxy Evolution, eds. J. S. Mulchaey, A. Dressler, & A. Oemler (Cambridge University Press), 305
van Haarlem, M. P., Wise, M. W., Gunst, A. W., et al. 2013, A&A, 556, A2
Venturi, T., Giacintucci, S., Merluzzi, P., et al. 2022, A&A, 660, A81
Vollmer, B., Cayatte, V., Balkowski, C., & Duschl, W. J. 2001, ApJ, 561, 708
Vollmer, B., Beck, R., Kenney, J. D. P., & van Gorkom, J. H. 2004, AJ, 127, 3375
Vollmer, B., Soida, M., Braine, J., et al. 2012, A&A, 537, A143
Vollmer, B., Soida, M., Beck, R., et al. 2013, A&A, 553, A116
Vulcani, B., Poggianti, B. M., Gullieuszik, M., et al. 2018, ApJ, 866, L25
Vulcani, B., Poggianti, B. M., Tonnesen, S., et al. 2020, ApJ, 899, 98
Vulcani, B., Poggianti, B. M., Smith, R., et al. 2022, ApJ, 927, 91
Waldron, W., Sun, M., Luo, R., et al. 2023, MNRAS, 522, 173
Watts, A. B., Cortese, L., Catinella, B., et al. 2023, PASA, 40, E017
Wenger, M., Ochsenbein, F., Egret, D., et al. 2000, A&AS, 143, 9
York, D. G., Adelman, J., Anderson, J. E., Jr., et al. 2000, AJ, 120, 1579
Yuan, Q., Zhou, X., & Jiang, Z. 2003, ApJS, 149, 53